Title

Reciprocity relations in a biologically inspired nanomagnonic system with dipolar coupling

Permalink

https://escholarship.org/uc/item/36m1h4cc

Journal

Applied Physics Letters, 124(13)

ISSN

0003-6951

Authors

Zingsem, Benjamin W

Feggeler, Thomas

Spoddig, Detlef

et al.

Publication Date

2024-03-25

DOI

10.1063/5.0195215

Peer reviewed

Title: Reciprocity relations in a biologically inspired nanomagnonic system with dipolar coupling

Authors: Benjamin W. Zingsem[1], Thomas Feggeler[2,3], Detlef Spoddig[4], Ralf Meckenstock[4], Michael Farle[4], Michael Winklhofer[5,6,a)]

Author affiliations:
[1]Ernst-Ruska Centre for Microscopy and Spectroscopy with Electrons, Forschungszentrum Jülich, 52428 Jülich, Germany
[2]Department of Physics, University of California, Berkeley, Berkeley CA 94720, United States
[3]Advanced Light Source, Lawrence Berkeley National Laboratory, Berkeley CA 94720, United States
[4]Faculty of Physics and Center for Nanointegration Duisburg-Essen (CENIDE), University of Duisburg-Essen, 47048 Duisburg, Germany
[5]Institut für Biologie und Umweltwissenschaften, Carl von Ossietzky Universität Oldenburg, 26129 Oldenburg, Germany
[6]Forschungszentrum Neurosensorik, Carl von Ossietzky Universität Oldenburg, 26111 Oldenburg, Germany

a) Author to whom correspondence should be addressed: michael.winklhofer@uol.de

Abstract

Magnetosome chains in magnetotactic bacteria present ideal nanomagnonic model systems for studying collective resonance modes of dipolar-coupled single domain particles in relation to their spatial arrangement. Using microresonator-based ferromagnetic resonance (FMR) spectroscopy, electron microscopy, and micromagnetic modelling, we here provide insights into the complex magnonic activity within a single magnetosome chain. While the angular dependence of its FMR spectrum is dominated by 2-fold symmetry features due to the uniaxial anisotropy of linear chain segments, we also observed unexpected behavior such as interrupted lines and flat bands due to the intricate geometrical details of this particular chain, such as a cross-like structural anomaly where a pair of particles is oriented perpendicular to the main axis of the chain and thus breaks the prevailing axial dipolar coupling symmetry. Such a cross junction formed by four particles exhibits interesting magnonic network properties, notably reciprocity in the sense that the spectral response of particle A given an excitation of particle B is identical to the response of particle B given an excitation of particle A. Furthermore, we have identified that magnonic coupling between A and B can be facilitated via a dark state, as in magnonic stimulated Raman adiabatic passage, and that this dark-state coupling can be made non-reciprocal between A and B by breaking the symmetry of the spatial arrangement of the four particles.

Main Text

Magnetotactic bacteria produce intracellular membrane-enclosed magnetic particles called magnetosomes and do so in a strictly biologically controlled way, yielding single-domain magnetic

particles with consistent shapes and sizes. Therefore, they present a rich platform for multidisciplinary research [Gan2023, She2023, Chen2018, Fai2008], opening avenues for advanced material science [Chen2018, Kör2014, Lan2007] and electron [Gan2023, Bar2013, Isa2007, Sim2005, Dun2001, Dun1998] and X-ray [Che2021, Feg2021, Mar2022, Zhu2016, Lam2010] microscopy studies. The magnetosomes are arranged in the form of chains, with the magnetic polarity of each particle summing up coherently to yield the maximum possible cellular magnetic dipole moment, instrumental in guiding the whole cell along geomagnetic field lines, referred to as magnetotaxis [Fra1979]. Intriguingly, these chains of dipolar coupled particles exhibit a richness of magnonic behaviors, which invites concepts for spin-wave devices operating at the nanoscale [Bar2021, Zing2019].

In this study, we focus on the magnonic properties of a single magnetosome chain, measured at room temperature with angular-dependent ferromagnetic resonance (FMR) spectroscopy using a microresonator [Nar2005, Nar2008] operated at 8.87 GHz. The precision of these measurements allows for the identification of both individual particle modes and collective resonance modes, a phenomenon that remains underexplored in existing literature, due to the limited sensitivity of conventional broadband and resonator based FMR. Using the chain geometry reconstructed from electron microscopy, we micromagnetically simulate the magnonic behavior to understand the magnonic activity within this biological structure. It turns out that the most fascinating behavior is generated by a cross-like structural anomaly in the chain, where a pair of magnetite nanoparticles is arranged perpendicular to the chain axis. Simulating excitation-response matrices for four particles in cross-like arrangement, we find interesting reciprocity relations, dark state coupling, and magnonic stimulated Raman adiabatic passage (StiRAP), which was described recently in magnonic wave guides [Wang2021].

For our experiment, we used cells of magnetotactic bacteria commercially available in pure culture (*Magnetospirillum gryphiswaldense* [Schl1991] strain MSR-1). Cells were transferred into a HEPES buffer, suctioned into a pipette, and dropped on a TEM carbon-coated copper grid. The grid was transferred into an FEI Helios NanoLabTM 600 Dual-beam FIB/SEM system to mill out a patch of the carbon film featuring an isolated single cell. The excised carbon film with the cell was placed inside the loop of a μ-resonator [Nar2008], thereby ascertaining that the μ-resonator was loaded with a single cell containing a single magnetosome chain (Fig. 1a).

The microresonator-based angular dependent Ferromagnetic Resonance (FMR) measurements were performed at 8.87 GHz and 50 mW input power using a custom-built continuous wave X-band FMR spectrometer consisting of a rotatable electromagnet, a Hall probe, and a Varian E-102 microwave bridge. The setup measures the microwave power reflected off the μ-resonator with a microwave detector integrated into the microwave bridge. For improved FMR sensitivity, the detected voltage is recorded by a Stanford Research SR 830 lock-in amplifier using as reference the signal of an incorporated field modulation at 123.45 Hz and 0.5 mT amplitude, which overlays the static DC magnetic field. The DC field was swept from 200 to 400 mT in steps of 0.5 mT with the resonator's in-plane orientation altered in a range of 180 degrees by 1-degree steps.

Micromagnetic Simulations were performed using the GPU-accelerated simulation software Mumax3

[Van2014, Exl2014]. The overall FMR spectrum of the magnetosome chain was simulated using a sinc-pulse excitation [Zing2019] to enhance performance. Additionally, we validated our results with a continuous wave (CW) type simulation (see SI for simulation details). Both simulations reveal the magnonic ground state spectrum ($k = 0$), i.e., the ferromagnetic resonance spectrum of the particle chain. The key difference is that in the sinc-pulse excitations mode scattering cannot be distinguished, as all modes are excited equally with a broad spectral pulse. In the CW excitation, on the other hand, individual modes are excited by applying continuous wave signals at fixed frequencies. In both excitation modes, the overall angular dependency of the simulated FMR spectra is identical, along with the typical features of multiple modes and mode interruptions.

Additional simulations were performed on a junction composed of four particles; a highly symmetric representation of the central area of the magnetosome chain (highlighted in red in Fig. 1a). We focussed on the spectral response S_{ij} of particle i to a selective sinc-pulse excitation of particle j ($i, j = 1 \dots 4$). Further, we modelled the responses of this entire ensemble ($i = 0$) to excitations of individual particles ($j = 1 \dots 4$) and, vice versa, the responses of individual particles ($i = 1 \dots 4$) to excitations of the entire ensemble ($j = 0$). The complete S_{ij} matrix thus has a 5 x 5 structure. Identical simulations were performed on a less symmetric representation of this junction.

The sample (Fig. 1a) from which we recorded angular dependent FMR spectra (Fig 1b) was a magnetosome chain composed of ca. 20-30 crystals of magnetite (ca 25 nm diameter), spaced apart by about 5 nm, with a total chain length of approximately 1 μm. The FMR lines are very narrow (ca. 1 mT, see Fig. S1c), indicating exceptionally small damping compared to synthetic magnetite thin films deposited on substrates [Roy2023]. The simulated FMR spectrum (Fig.1c) of the chain model (depicted at the bottom of Fig. 1) allows us to identify the origin of some features in the experimental spectrum. For this purpose, we have colored the spectral lines from the simulation according to the particle that contributes most to it (Fig. 1d). It can be seen that the major axis of the chain produces the line with the strongest intensity and largest anisotropy, following a 2-fold symmetry induced by the overall shape anisotropy of the chain. In contrast, the short segment – bent away from the main axis at the upper end – gives rise to the resonance line (shown in dark blue in Fig. 1d), which is offset by ca. 60° from the main line but still has 2-fold symmetry, albeit with a weaker anisotropy due to the comparatively short length of that segment.

From the micromagnetic simulations, we find that the particle size is sufficiently small to suppress edge modes [Wang2019, Zing2019]. Each particle behaves as a single oscillator, responding only with a $k = 0$ mode (uniform oscillation). At the same time, the entire chain exhibits modes of $k \neq 0$, where neighboring oscillators respond at a different phase, minimizing the dipolar energy of the coupled system and effectively forming a standing wave envelope across multiple particles.
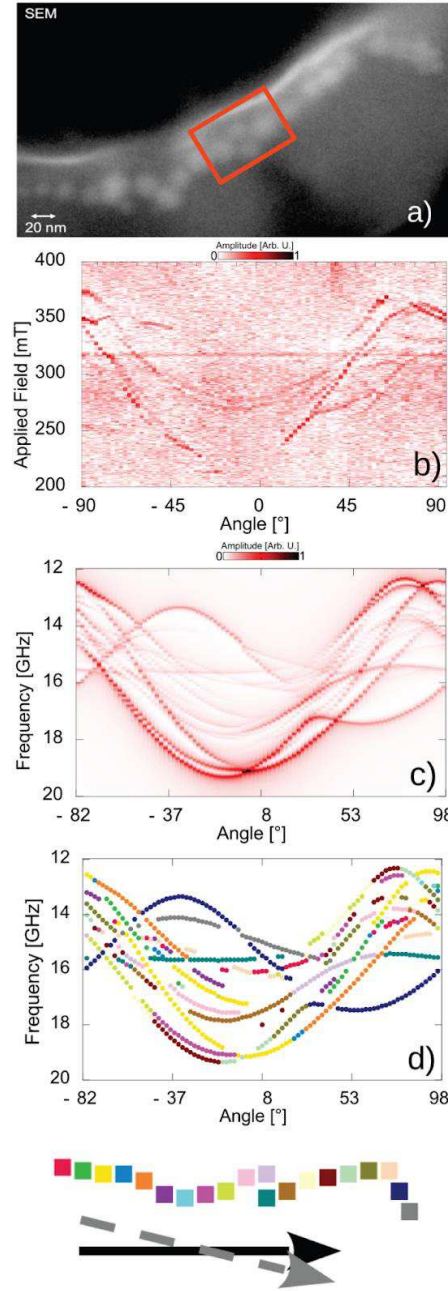
Figure 1: Sample and FMR Spectra:

a) SEM micrograph of the magnetosome chain still encapsulated by the bacteria cell, as used in the FMR experiments. The rectangle highlights the 4-particle junction in the center of the chain.

b) FMR spectrum of the chain, recorded at 8.87 GHz. The grey dashed arrow (bottom right) shows the direction corresponding to 0°, relative to the chain.

c) Frequency-dependent FMR spectrum obtained from sinc-type micromagnetic simulations at an applied field of 600 mT. The Field was rotated clockwise. The black arrow to the right shows the direction corresponding to 0°.

d) For each particle in the model, a color was assigned (compare the model to the right). At each resonance detected in c), a point was placed with the color corresponding to that particle in the chain, contributing to this resonance with the highest amplitude.

While the overall symmetry of the spectrum in Fig. 1 b) and d) displays a 2-fold symmetry, intricate details of the chain geometry give rise to interesting phenomena. In particular, individual resonance lines are not only offset to the overall 2-fold symmetry but bear completely different angular dependencies. This includes distortions of the resonance's angular-dependent symmetry, avoided crossings, and spectral interruptions, which were previously [Zing2019] identified to be due to the commensurability of the magnonic ground states in different segments. Hence, to understand the features of the spectrum in detail, the exact geometric composition of the chain has to be considered. As a first step towards a full understanding of this complex magnonic coupling, we focus here on the cross-like substructure near the center of the chain (highlighted in red in Fig. 1a), due to a pair of particles oriented perpendicular to the main axis of the chain. This pair breaks the prevailing axial dipolar coupling symmetry. To illustrate the spectral responses to stimuli of different localization, we have computed the four-port S_{ij} matrix of a highly symmetric cross-like junction (Fig. 2), in comparison to a maximally asymmetric junction (Fig. 3) as a more realistic representation of the actual chain geometry.

For the case of the highly symmetric cross-like junction, one can see that a spatially uniform excitation (left column in Fig. 2) produces two modes (S_{00}), one dominated by the responses of the outer particles (S_{10} and S_{40}), the other one dominated by the response of the inner particles (S_{20} and S_{30}), the latter becoming somewhat attenuated as the field angle approaches the long axis of the junction. Band gaps appear in each spectrum where high energy and low energy modes repel each other because of incompatible spatial mode profiles [Zing2019, Bar2021]. When looking at the symmetry properties of the S_{ij} matrix, we find that the spectral characteristics obey reciprocity in the sense that the spectral response S_{ij} of particle $i = \mu$ due to an excitation of particle $j = \nu$ is identical to that of particle $j = \mu$ to excitation of particle $i = \nu$, i.e., $S_{ji} = S_{ij}$. This is contrary to the naive assumption that the resonant properties of a particle are solely determined by its local dipolar environment. This view only holds when a given particle responds to an excitation of that same particle (compare the diagonal S_{ii}). If, however, the excitation is mediated via dipolar coupling and through additional particles, then the available modes are filtered, and as a result, reciprocity among the spectra is established.

To confirm that spectral reciprocity is not an artificial property of the highly symmetric geometry of the junction depicted in Fig. 2, but a general aspect of a magnonic circuit based on dipolar coupling, we have performed the same type of simulation on an asymmetric four-particle junction (Fig. 3). Importantly, the reciprocity $S_{ij} = S_{ji}$ is reproduced, despite the broken symmetry. However, the second symmetry plane formed by the antidiagonal of the lower right 4 x 4 submatrix of the symmetric configuration ($S_{11} = S_{44}, S_{22} = S_{33}, S_{12} = S_{34}$ etc. in Fig. 2), is absent from the S matrix of the asymmetric configuration (Fig. 3), and therefore the 2-fold rotation symmetry of the submatrix disappears, too. Likewise, the mirror symmetries apparent in Fig. 2 ($S_{13} = \check{S}_{12}, S_{31} = \check{S}_{21}, S_{24} = \check{S}_{34}, S_{42} = \check{S}_{43}$, with $\check{S}(\varphi) = S(\pi - \varphi)$) are no longer present in the asymmetric configuration (Fig. 3).
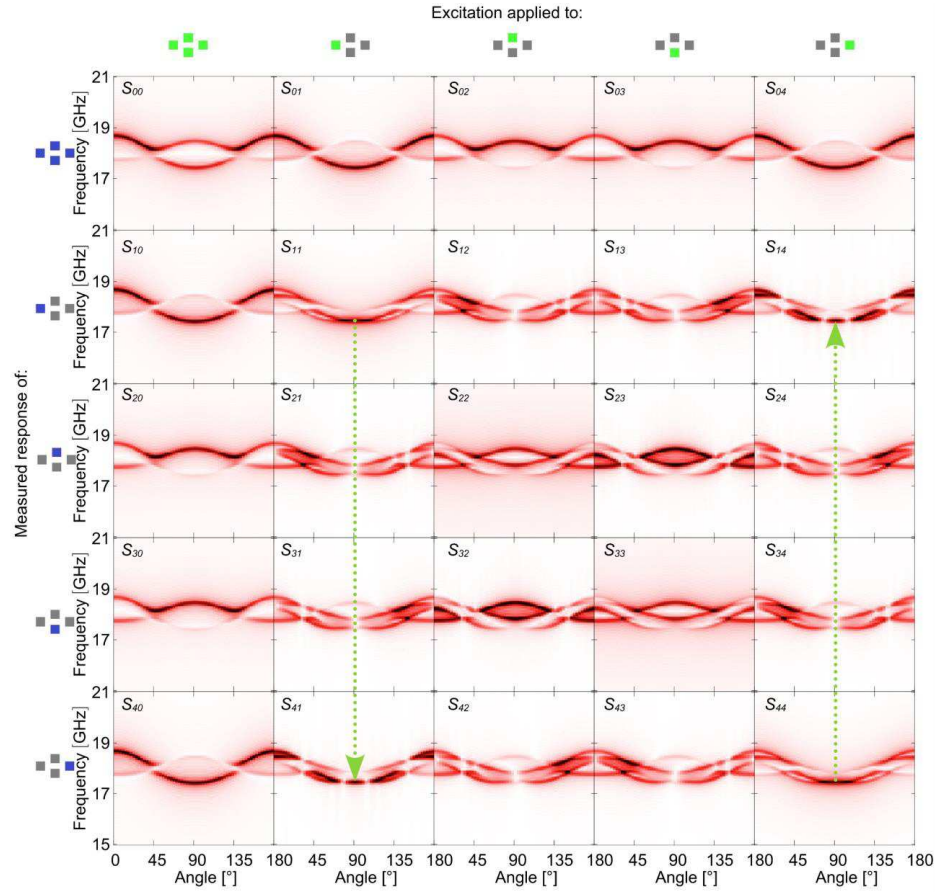
Figure 2: Simulation of spectral response of the central junction in the chain. S_{i0}: Angular-dependent frequency components of the magnonic response to a uniform sinc-pulse excitation applied to the entire ensemble. S_{00}: Response of the entire particle ensemble. S_{10} - S_{40}: Individual responses of each of the constituent particles (highlighted in green in the inset). S_{i1}: Sinc-pulse excitation applied to the leftmost particle. S_{11} - S_{41}: Individual responses of each of the constituent particles. S_{i2}: Sinc-pulse excitation applied to the particle located top center. S_{12} - S_{42}: Individual responses of each of the constituent particles. S_{i3}: Sinc-pulse excitation applied to the particle located bottom center. S_{13} - S_{43}: Individual responses of each of the constituent particles. S_{i4}: Sinc-pulse excitation applied to the particle on the right. S_{14} - S_{44}: Individual responses of each of the constituent particles. See Fig. S3 and S5 in SI material for simulations of the symmetric junction with random and uniform MAE, resp.
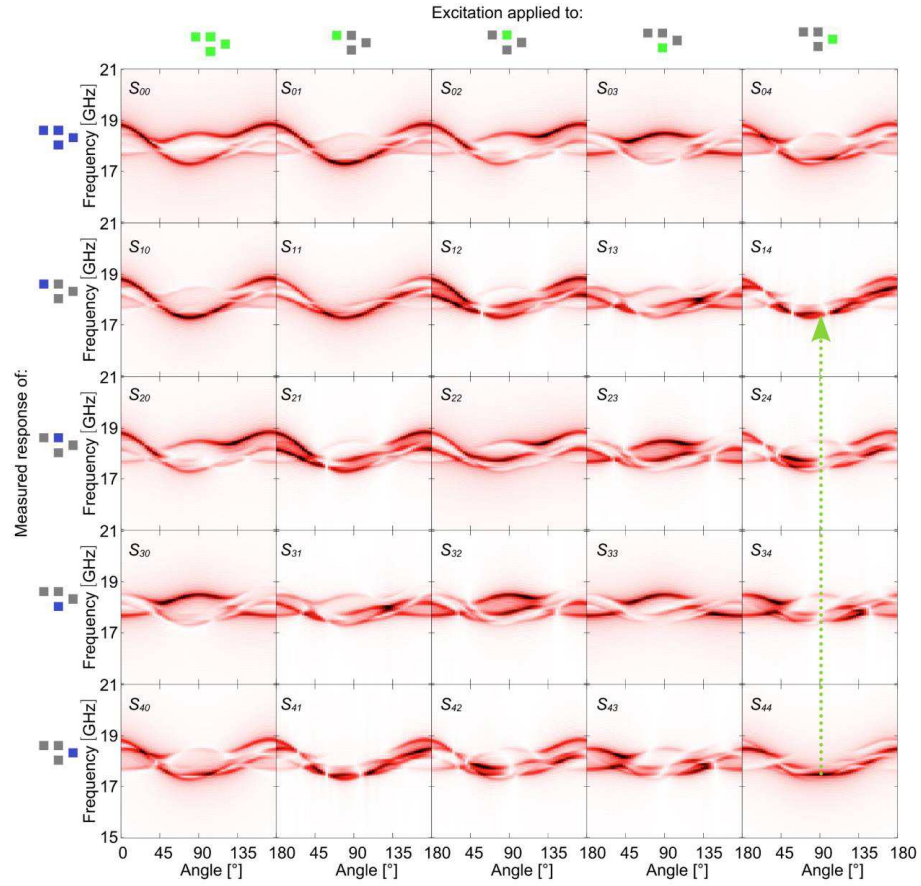
Figure 3: Effects of geometrical symmetry break on standing wave spectrum: S_{i0}: Angular-dependent frequency components of the magnonic response to a uniform sinc-pulse excitation applied to the entire ensemble. S_{00}: Response of the entire particle ensemble. S_{10} - S_{40}: Individual responses of each of the constituent particles (highlighted in green in the inset). S_{i1}: Sinc-pulse excitation applied to the leftmost particle. S_{11} - S_{41}: Individual responses of each of the constituent particles. S_{i2}: Sinc-pulse excitation applied to the particle located top center. S_{12} - S_{42}: Individual responses of each of the constituent particles. S_{i3}: Sinc-pulse excitation applied to the particle located bottom center. S_{13} - S_{43}: Individual responses of each of the constituent particles. S_{i4}: Sinc-pulse excitation applied to the particle on the right. S_{14} - S_{44}: Individual responses of each of the constituent particles. See Fig. S4 and S6 in SI material for simulations of the asymmetric junction with random and uniform MAE, resp.

To test if reciprocity $S_{ij} = S_{ji}$ generally holds in a dipolarly coupled system, we next included the cubic magnetocrystalline anisotropy energy (MAE) term, which we deliberately neglected thus far. To break the symmetry maximally, we varied the orientation of the cubic <100> axes system randomly from one particle to the next ("random MAE"). As a control, we oriented the <100> axes always parallel to the surface normals of the cube-shaped particles ("uniform MAE"). In Figures S3 to S6 of the SI material, one can clearly see that the addition of MAE produces different spectra compared to their MAE-free counterparts in Fig. 2 and Fig. 3. The pronounced effect of MAE on the spectra of the junction can be explained by its compact geometry, having a much less pronounced shape anisotropy compared to a magnetosome chain (where shape anisotropy dominates over MAE energy). Most importantly though, the coupling matrices always are symmetric about the main diagonal and thus reciprocity $S_{ij} = S_{ji}$ is retained, even in the case of random MAE (Figs. S3, S4). The only change observed concerns the symmetry about the antidiagonal of the matrix for the symmetric junction (compare Fig. 2 with Fig. S3), which is broken in the case of random MAE (Fig. S3). Interestingly, both for the symmetric junction (Fig. S5) and asymmetric junction (Fig. S6), the symmetry properties of the coupling matrix S_{ij} are invariant to the uniform addition of MAE, with S_{ij} of the symmetric junction being symmetric about the antidiagonal (compare Fig. S5 with Fig. 2).

Another interesting feature observed in the symmetric junction can be seen in Fig. 2 (and in Fig. S5) in column $j = 1$ at an applied field angle of 90°, i.e., parallel to the short axis connecting the two inner particles (green arrow in Fig. 2). Here, the left particle can only be excited near 17.5 GHz (low frequency mode of S_{11} at 90°in Fig. 2). In this very spectral range, the angular dependent modes of S_{21} and S_{31} are interrupted, which means each of the two inner particles forms a dark state in the magnonic eigenstate of the system. The state remains unpopulated (dark) in the inner particles, that is, they do not resonate, but nonetheless mediate magnonic coupling between the outer particles. Still, the right particle responds to the excitation of the left particle at the same frequency (S_{41} in Fig. 2). Coupling between the two end magnetic particles across a dark state is similar to the magnonic StiRAP described in [Wang2021]. Regardless of the dark state, the essential role of the inner particles is to mediate strong magnetostatic coupling and thereby facilitate magnonic coupling between the outer particles. This can be seen in a control simulation for just the two outer particles, resulting in single-band spectra without pronounced angular dependence (Fig. S7). Another spectral feature in the angular range about 90° is the presence of a high energy mode at 18.5 GHz (albeit of low spectral amplitude) in S_{21} and S_{31}, which is not present in S_{11} and S_{41} (Fig. 2). Here energy from the single-particle excitation of the input particle at a lower frequency of 17.5 GHz is scattered into the higher frequency mode. The mode behavior is observed in S_{12} except here, a mode at the relevant energy is provided by the input particle as shown in S_{22}. For symmetry reasons, column $j = 4$ (Fig. 2) shares the same features as column $j = 1$, except that now the rightmost particle is being excited. Columns $j = 2,3$ in Fig. 2 show that energy transfer between the inner particles (S_{32} and S_{23}) at 90° can occur with or without populating bands in the end particles, depending on whether the mode at higher or lower energy is selected.

In the asymmetric junction, the dark state is still visible as a clear interruption of the angular dependent resonances in the central particles (S_{24} and S_{34} in Fig. 3). However, owing to the broken symmetry ($S_{24} \neq \check{S}_{34}$), the spectral gap here is not symmetric and the dark state is populated to some extent

(compare green arrow in Fig. 3). By comparing column $j = 4$ with $j = 1$ (Fig. 3), it can be seen that the dark-state coupling in the perturbed geometry is non-reciprocal in space. This is due a loss of the 2-fold rotation symmetry of the 4x4 submatrix, which in the symmetric arrangement ($S_{21} = S_{34}, S_{31} = S_{24}$ in Fig. 2) ascertained the spatial reciprocity of the dark-state coupling.

In summary, inspired by the ferromagnetic resonance spectrum of a biogenic assembly of magnetic nanoparticles, we have shown the presence of magnon-circuit reciprocity and magnonic dark state coupling, and how it can be tuned via the geometry of the arrangement. Our FMR measurements confirm the magnonic response of the system and its symmetry. Using micromagnetic modeling, we reproduce the principal features of the measured FMR spectrum. Further micromagnetic modeling of the 4-particles at the junction in the center of the magnetosome chain reveals magnonic circuit reciprocity, namely the spectral properties measured at point A in the system, given an excitation at point B is equal to the spectral properties at point B, given an excitation at point A. Furthermore, we have identified that, in such an assembly, magnonic coupling can be facilitated via a dark state, i.e., the lack of magnonic excitation in the part of the system through which the magnonic coupling is mediated between two points. We have also shown that this coupling can be made nonreciprocal, in the sense that an excitation at point A that leads to a magnonic response at point B can couple via a dark state, while the same excitation at point B, leading to the respective response at A can be mediated through regular magnonic excitation of the particles between A and B. This last point has been achieved by breaking the spatial (mirror and rotational) symmetry of the geometric arrangement.

Supplementary Material

Further information on experimental and numerical methods used as well as results from control simulations are available in the supplementary material linked to this article.

Acknowledgments

Authors declarations

The authors declare no conflict of interest. Author contributions: BZ, MW: designed research; RM, DS performed experimental work; BZ, TF: performed simulations and sample preparation; BZ: processed data; BZ, MW: analyzed data; BZ wrote most of the paper with contributions from DS, RM, TF, MW. All authors discussed the results and approved the manuscript.

Data availability statement:

Data are availabe at https://osf.io/v7m2n/?view_only=1406e6a38d8241109eef07a3f2908c58

References

[Gan2023] D. Gandia, L. Marcano, L. Gandarias, D. Villanueva, I. Orue, R. M. Abrudan, S. Valencia, I. Rodrigo, J. Á. García, A. Muela, M. L. Fdez-Gubieda, and J. Alonso, Tuning the magnetic response of magnetospirillum magneticum by changing the culture medium: a straightforward approach to improve their hyperthermia efficiency, *ACS Appl. Mater. Interf.* **15**, 566–577 (2023).

[She2023] J. Shen, G. A. Paterson, Y. Wang, J. L. Kirschvink, Y.-X. Pan and W Lin, Renaissance for magnetotactic bacteria in astrobiology, *ISME J.* **17**, 1526–1534 (2023).

[Chen2018] H. Chen, S. D. Zhang, L. Chen, Y. Cai, W. J. Zhang, T. Song, and L.-F- Wu, Efficient genome editing of Magnetospirillum magneticum AMB-1 by CRISPR-Cas9 system for analyzing magnetotactic behavior, *Front. Microbiol.* **9**, 1569 (2018).

[Fai2008] D. Faivre and D. Schüler, Magnetotactic bacteria and magnetosomes, *Chem. Rev.* **108**, 4875 (2008).

[Kör2014] A. Körnig, M. Winklhofer, J, Baumgartner, T. Perez Gonzalez, P. Fratzl, and D. Faivre, Magnetite crystal orientation in magnetosome chains, *Adv. Funct. Mater.* **24**, 3926–3932 (2014).

[Lan2007] C. Lang, D. Schüler, and D. Faivre, Synthesis of magnetite nanoparticles for bio- and nanotechnology: Genetic engineering and biomimetics of bacterial magnetosomes, *Macromol. Biosci.* **7**, 144-151 (2007).

[Bar2013] D. A. Bazylinski and C. T. Lefèvre, Magnetotactic bacteria from extreme environments, *Life* **3**, 295-307 (2013).

[Isa2007] A. Isambert, N. Menguy, E. Larquet, F. Guyot, and J.-P. Valet, Transmission electron microscopy study of magnetites in a freshwater population of magnetotactic bacteria, *Am. Miner.* **92**, 621–630 (2007).

[Sim2005] E. T. Simpson, T. Kasama, M. Pósfai, P. R. Buseck, R. J. Harrison, and R. E. Dunin-Borkowski, Magnetic induction mapping of magnetite chains in magnetotactic bacteria at room temperature and close to the Verwey transition using electron holography, *J. Phys.: Conf. Ser.* **17**, 108 (2005).

[Dun2001] R. E. Dunin-Borkowski, M. R. Mccartney, M. Pósfai, R. B. Frankel, D. A. Bazylinski, and P. R. Buseck, Off-axis electron holography of magnetotactic bacteria : magnetic microstructure of strains MV-1 and MS-1, *Eur. J. Miner.* **13**, 671–684 (2001).

[Dun1998] R. E. Dunin-Borkowski, M. R. Mccartney, R. B. Frankel, D. A. Bazylinski, M. Pósfai, and P. R. Buseck, Magnetic microstructure of magnetotactic bacteria by electron holography, *Science* **282**, 5395 (1998).

[Mar2022] L. Marcano, I. Orue, D. Gandia, L. Gandarias, M. Weigand, R. M. Abrudan, A. Garcia-Prieto, A. Garcia-Arribas, A. Muela, M. L. Fdez-Gubieda, and S. Valencia, Magnetic anisotropy of individual nanomagnets embedded in biological systems determined by axi-asymmetric X-ray transmission microscopy, *ACS Nano* **16**, 7398-7408 (2022).

[Che2021] D. M. Chevrier, E. Cerdá-Doñate, Y. Park, F. Cacho-Nerin, M. Gomez-Gonzalez, R. Uebe, and D. Faivre, Synchrotron-based nano-X-ray absorption near-edge structure revealing intracellular heterogeneity of iron species in magnetotactic bacteria, *Small Sci.* **2**, 2100089 (2021).

[Feg2021] T. Feggeler, R. Meckenstock, D. Spoddig, B. W. Zingsem, H. Ohldag, H. Wende, M. Farle, M. Winklhofer, and K. J. Ollefs, Spatially resolved GHz magnetization dynamics of a magnetite nano-particle chain inside a magnetotactic bacterium, *Phys. Rev. Res.* **3**, 033036 (2021).

[Zhu2016] X. H. Zhu, A. P. Hitchcock, D. A. Bazylinski, P. Denes, J. Joseph, U. Lins, S. Marchesini, H.-W. Shiu, T. Tyliszczak, and D. A. Shapiro, Measuring spectroscopy and magnetism of extracted and intracellular magnetosomes using soft X-ray ptychography, *Proc. Nat. Acad. Sci. U.S.A.* **113**, E8219-E8227 (2016).

[Lam2010] K. P. Lam, A. P. Hitchcock, M. Obst, J. R. Lawrence, G. D.W. Swerhone, G. G. Leppard, T. Tyliszczak, C. Karunakaran, J. Wang, K. Kaznatcheev, D. A. Bazylinski, and U Lins, Characterizing magnetism of individual magnetosomes by X-ray magnetic circular dichroism in a scanning transmission X-ray microscope, *Chem. Geol.* **270**, 110-116 (2010).

[Fra1979] R. B. Frankel, R. Blakemore, and R. S. Wolfe, Magnetite in freshwater magnetotactic bacteria, *Science* **203**, 1355-1356 (1979).

[Bar2021] A. Barman, G. Gubbiotti, S. A. Nikitov et al. The 2021 magnonics roadmap, *J. Phys. Cond. Mat.* **33**, 413001 (2021).

[Zing2019] B. W. Zingsem, T. Feggeler, A. Terwey, S. Ghaisari, D. Spoddig, D. Faivre, R. Meckenstock, M. Farle, and M. Winklhofer, Biologically encoded magnonics, *Nat. Commun.* **10**, 4345 (2019).

[Wang2021] Q. Wang, T. Brächer, M. Fleischhauer, B. Hillebrands, P. Pirro, Stimulated-Raman-adiabatic-passage mechanism in a magnonic environment, *Appl. Phys. Lett.* **118**, 182404 (2021)

[Wang2019] Q. Wang, B. Heinz, R. Verba, M. Kewenig, P. Pirro, M. Schneider, T. Meyer, B. Lägel, C. Dubs, T. Brächer, and A. V. Chumak, Spin pinning and spin-wave dispersion in nanoscopic ferromagnetic waveguides, *Phys. Rev. Lett.* **122**, 247202 (2019)

[Van2014] A. Vansteenkiste, J. Leliaert, M. Dvornik, M. Helsen, F. Garcia- Sanchez, and B. Van Waeyenberge, The design and verification of MuMax3, *AIP Adv.* **4**, 107133 (2014).

[Exl2014] L. Exl, S. Bance, F. Reichel, T. Schrefl, H. P. Stimming, and N. J. Mauser, LaBonte's method revisited: an effective steepest descent method for micromagnetic energy minimization, *J. Appl. Phys.* **115**, 17D118 (2014).

[Nar2005] R. Narkowicz, D. Suter, and R. Stonies, Planar microresonators for EPR experiments, *J. Magn. Reson.* **175**, 275 (2005).

[Nar2008] R. Narkowicz, D. Suter, and I. Niemeyer, Scaling of sensitivity and efficiency in planar microresonators for electron spin resonance, *Rev. Sci. Instr.* **79**, 084702 (2008).

[Schl1991] K. H. Schleifer, D. Schüler, S. Spring, M. Weizenegger, R. Amann, W. Ludwig, and M. Köhler, The genus Magnetospirillum gen. nov., description of *Magnetospirillum gryphiswaldense* sp. nov., and transfer of *Aquaspirillum magnetotacticum* to *Magnetospirillum magnetotacticum* comb. nov., *Syst. Appl. Microbiol.* **14**, 379 (1991).

[Roy2023] J. Roy, P. R. Teja, S. Sahu, G. A. Basheed and R. B. Gangineni, Influence of in-situ annealing temperature upon structural, micro-structural, magnetic damping properties in sputtered Fe_3O_4 thin films, *J. Magn. Magn. Mater.* **585**, 171130 (2023).